


Cite this: *Polym. Chem.*, 2024, **15**,  
2763

# Design of poly(*N*-isopropylacrylamide) coated MnO<sub>2</sub> nanoparticles for thermally regulated catalytic decomposition of H<sub>2</sub>O<sub>2</sub>†

Anashwara Babu,‡<sup>a</sup> Samarendra Maji,\*‡<sup>a,b</sup> Gomathi Sivakumar<sup>a</sup> and  
Richard Hoogenboom  \*<sup>b</sup>

We report the synthesis of thermoresponsive poly(*N*-isopropylacrylamide) (PNIPAM) coated manganese dioxide nanoparticles (PNIPAM@MnO<sub>2</sub> NPs) for the catalytic decomposition of hydrogen peroxide (H<sub>2</sub>O<sub>2</sub>), with the goal of developing a temperature-controlled catalytic system. For this purpose, we have developed MnO<sub>2</sub> NPs and further modified them with thermoresponsive PNIPAM containing nitrodopamine end groups. The modification of the MnO<sub>2</sub> NPs was confirmed using SEM, TEM, XPS, and TGA. Upon varying the temperature above and below the lower critical solution temperature (LCST) of the polymer coating, the NPs undergo spontaneous cyclic swelling–deswelling changes, as confirmed by DLS measurements. Photoluminescence (PL) experiments were performed to explore the catalytic decomposition of H<sub>2</sub>O<sub>2</sub> by PNIPAM@MnO<sub>2</sub> NPs, indicating thermal control over the catalytic activity of the MnO<sub>2</sub> NPs. The proposed proof-of-concept of these smart PNIPAM@MnO<sub>2</sub> NPs for the decomposition of H<sub>2</sub>O<sub>2</sub> may serve as a basis for the development of smart catalytic self-regulating systems in future work.

Received 31st May 2024,  
Accepted 15th June 2024

DOI: 10.1039/d4py00595c

rsc.li/polymers

## Introduction

Hydrogen peroxide (H<sub>2</sub>O<sub>2</sub>) catalysis plays a crucial role in biological processes as well as various chemical processes including the production of detergents, bleaching agents, and rocket propellants.<sup>1,2</sup> H<sub>2</sub>O<sub>2</sub> naturally decomposes into water (H<sub>2</sub>O) and oxygen (O<sub>2</sub>) over time, but this process can be expedited and controlled by introducing a catalyst. The catalytic decomposition of H<sub>2</sub>O<sub>2</sub> holds immense importance in laboratory chemical reactions due to its ability to serve as a controlled source of oxygen.<sup>3,4</sup> Common catalysts for this purpose include transition metal ions, such as manganese (Mn), iron (Fe), and palladium (Pd).<sup>5–8</sup> The controlled release of oxygen in chemical reactions is valuable for enhancing reaction rates and promoting specific pathways, making catalytic decompo-

sition a key aspect of numerous chemical and biochemical processes such as oxidation reactions and the synthesis of organic compounds.<sup>9</sup> Understanding the importance of H<sub>2</sub>O<sub>2</sub> catalysis in biological systems provides insights into the delicate balance of cellular processes and may hold implications for therapeutic interventions in diseases associated with oxidative stress.<sup>10</sup> Enzymes such as peroxidases and catalases catalyze the decomposition of H<sub>2</sub>O<sub>2</sub> in the biological domain.<sup>11–13</sup> The controlled acceleration of this decomposition is crucial for maintaining cellular homeostasis. This process is vital in preventing the accumulation of toxic levels of H<sub>2</sub>O<sub>2</sub> within cells, as high concentrations can lead to oxidative stress and cellular damage.<sup>14</sup> Beyond detoxification, H<sub>2</sub>O<sub>2</sub> is also involved in signalling pathways, serving as a secondary messenger that regulates cellular functions. In particular, it is involved in the modulation of gene expression, immune response, and cell proliferation.<sup>14–16</sup> Additionally, certain metabolic pathways, such as fatty acid metabolism, utilize H<sub>2</sub>O<sub>2</sub> as a signalling molecule, emphasizing its multifaceted role in various biological activities.<sup>17</sup>

Typically, the primary determinant of catalytic efficiency in heterogeneous catalysis is sufficient crystallinity and expansive surface area, which are achievable through the utilization of either nanoparticles or granular particles exhibiting porous characteristics.<sup>18</sup> Hermanek *et al.*<sup>19</sup> conducted an extensive study on the effect of surface area and crystallinity of iron(III) oxides on the catalytic decomposition of H<sub>2</sub>O<sub>2</sub>. In a recent

<sup>a</sup>Department of Chemistry, Faculty of Engineering and Technology, SRM Institute of Science and Technology (SRMIST), Kattankulathur, Tamil Nadu-603203, India. E-mail: samarenr@srmist.edu.in

<sup>b</sup>Supramolecular Chemistry Group, Department of Organic and Macromolecular Chemistry, Ghent University, Krijgslaan 281 S4, Ghent, Belgium. E-mail: richard.hoogenboom@ugent.be

† Electronic supplementary information (ESI) available: <sup>1</sup>H NMR spectra of nitrodopamine hydrogensulfate, PFP containing CTA and nitro DOPA-CTA, SEC analysis for PNIPAM, pictorial representations, particle size, EDX, XPS, TGA and DLS for MnO<sub>2</sub> and PNIPAM@MnO<sub>2</sub> NPs, and photophysical properties with additional data. See DOI: <https://doi.org/10.1039/d4py00595c>

‡ These authors contributed equally to this work.



study, iron phosphide was loaded onto alumina to create 4–6 mm spheres that can activate  $\text{H}_2\text{O}_2$  and facilitate the decomposition of contaminants in wastewater.<sup>20</sup> Manganese dioxide nanoparticles ( $\text{MnO}_2$  NPs) have an attractive combination of stability, high catalytic efficiency, and cost-effectiveness that sets them apart from all other metal-based catalysts for  $\text{H}_2\text{O}_2$  decomposition.<sup>21,22</sup> Their importance lies not only in their catalytic activity but also in their biocompatibility and ability to operate under mild conditions. The unique structural features of  $\text{MnO}_2$  NPs, such as their high surface area and reactive sites, make them well-suited for interacting with  $\text{H}_2\text{O}_2$  efficiently.<sup>23</sup> Owing to the high reactivity of manganese dioxide ( $\text{MnO}_2$ ) towards hydrogen peroxide, it is used in fuel cells in space programs for the exothermic catalytic decomposition of  $\text{H}_2\text{O}_2$  for the sustained production of  $\text{O}_2$ .<sup>24</sup>

The decomposition of  $\text{H}_2\text{O}_2$  in chemical reactions is highly temperature-dependent, following the Arrhenius equation, which plays a crucial role in determining the reaction rate and pathway.<sup>25</sup> Understanding the complicated relationship between temperature and hydrogen peroxide decomposition can be vital for designing efficient and controlled reactions in diverse industrial and laboratory settings. Furthermore, the temperature-sensitive catalytic decomposition of  $\text{H}_2\text{O}_2$  provides a means to precisely control the levels of  $\text{H}_2\text{O}_2$  in biological environments. The temperature sensitivity ensures that the decomposition rates align with the dynamic nature of cellular processes, allowing for real-time adjustments in response to varying conditions. This temperature-dependent control is particularly relevant in disease states where fluctuations in temperature often accompany physiological changes. Conditions such as inflammation or infections, which are associated with altered temperatures, can benefit from tailored approaches that consider both the catalytic activity and temperature responsiveness of the decomposition process. This understanding opens avenues for developing targeted therapies that leverage temperature-sensitive catalysts to regulate hydrogen peroxide levels in a spatially and temporally controlled manner, which has not been explored much by researchers. A recent study from our group explained the efficient surface modification of  $\text{MnO}_2$  nanosheets by a nitrodopamine moiety for extracellular and intracellular glutathione detection.<sup>26</sup> This work inspired the utilization of a thermoresponsive polymer having a nitrodopamine end group for the surface modification of  $\text{MnO}_2$  NPs. Polymeric materials, especially thermoresponsive polymers [e.g. poly(*N*-isopropyl acrylamide) (PNIPAM)] that undergo a temperature-driven reversible phase transition [LCST] in aqueous solution, have been studied for the development of thermoresponsive smart materials.<sup>27</sup> Different metal/metal oxide nanoparticle (NP) cores with thermoresponsive PNIPAM have been investigated for the preparation of smart materials for diverse applications, such as sensors and actuators.<sup>28,29</sup>

These smart NPs have been prepared either *via* 'grafting to' or 'grafting from' approaches.<sup>30</sup> Polymers synthesized *via* controlled radical polymerization 'CRP' methods (atom transfer radical polymerization (ATRP),<sup>31–34</sup> nitroxide mediated

polymerization (NMP),<sup>35–37</sup> and reversible addition–fragmentation chain transfer (RAFT) polymerization) are extensively used for the modification of inorganic NPs as these methods provide ease of synthesis of polymers with precise molar masses, diverse compositions, and a high degree of chain-end functionality.<sup>38–44</sup> Among the CRP methods, RAFT polymerization is very appealing because of its compatibility with a vast array of monomers, mild reaction conditions and because it avoids the use of metal catalysts.<sup>43,45</sup> Thermoresponsive LCST polymers show a phase transition due to the change in entropy of solvation of the polymeric chain in aqueous solution as temperature alters.<sup>46</sup> PNIPAM is the most widely used thermoresponsive polymer having a sharp phase transition at around 32 °C.<sup>47–50</sup> Unlike existing studies that primarily focus on drug delivery or environmental applications by coating polymers on the surface of  $\text{MnO}_2$  NPs, this study highlights the thermoresponsive catalytic activity. Therefore, inorganic (metal/metal oxide) nanoparticles (NPs) with a temperature-regulating thermoresponsive polymer layer was hypothesized to enable temperature-responsive catalytic decomposition of  $\text{H}_2\text{O}_2$ .

By coating manganese dioxide nanoparticles with a temperature-responsive PNIPAM (PNIPAM@ $\text{MnO}_2$  NPs), the decomposition of  $\text{H}_2\text{O}_2$  might be controlled. The decomposition of  $\text{H}_2\text{O}_2$  takes place when the polymer is hydrated, which is at a temperature below the lower critical solution temperature (LCST) of PNIPAM, allowing  $\text{H}_2\text{O}_2$  to reach the manganese oxide catalytic nanoparticles, leading to its decomposition into water and oxygen. Thus,  $\text{H}_2\text{O}_2$  is no longer available for the dimerization of the non-fluorescent homovanillic acid as a model substrate into a fluorescent dimer. When the solution temperature rises over the polymer LCST, the polymer dehydrates and collapses onto the  $\text{MnO}_2$  NPs as a hydrophobic coating. Since in this state,  $\text{H}_2\text{O}_2$  cannot reach the catalytic surface due to the presence of the dehydrated polymer layer around the nanoparticles,  $\text{H}_2\text{O}_2$  is available for catalyzing the dimerization reaction, forming a fluorescent product, as shown in Fig. 1.

In this study, we will discuss the synthesis of thermoresponsive PNIPAM-coated  $\text{MnO}_2$  NPs and their use in the temperature controlled catalytic decomposition of  $\text{H}_2\text{O}_2$ , which may in the future be used as a basis for the design of smart catalytic self-regulating systems.

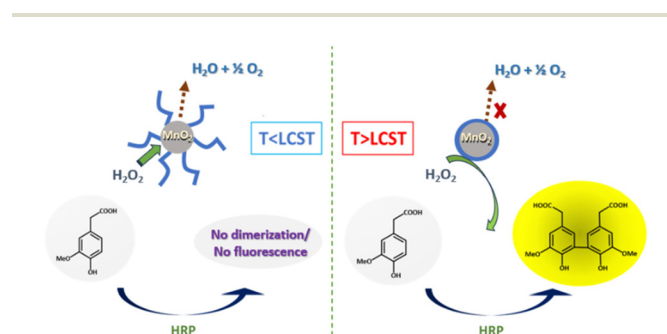


Fig. 1 Temperature-driven catalytic decomposition of  $\text{H}_2\text{O}_2$ .



## Experimental

### Materials

*N*-Isopropylacrylamide (NIPAM) was purchased from Scientific Polymer Products, INC., and was recrystallized twice from *n*-hexane before use. Potassium permanganate (KMnO<sub>4</sub>) and sodium nitrite (NaNO<sub>2</sub>) were obtained from Acros Organics Chemicals. Isoamyl alcohol was purchased from Ferak Berlin GmbH. Azobisisobutyronitrile (AIBN), pentafluorophenol (PFP), *N,N'*-dicyclohexylcarbodiimide (DCC), 4-dimethylaminopyridine (DMAP), dopamine hydrochloride, and sodium sulfate (Na<sub>2</sub>SO<sub>4</sub>) were obtained from Sigma Aldrich. AIBN was recrystallized from MeOH (twice) and stored in a freezer. A 2-(Butylthiocarbonothioylthio)propanoic acid (BTTCP) chain transfer agent was synthesized as previously reported.<sup>46</sup> HPLC grade organic solvents dichloromethane (DCM), chloroform (CHCl<sub>3</sub>), ethylacetate (EtOAc), dimethylformamide (DMF, anhydrous), *N,N*-dimethylacetamide (DMAc), and diethyl ether (DEE) were obtained from Sigma Aldrich. *N,N*-Dimethylformamide (DMF) was obtained from Biosolve and *n*-hexane was from Fischer Scientific. Trimethylamine (TEA) (dry) was purified and collected from the solvent purification system (SPS). Unless specified otherwise, all reagents and solvents were used exactly as purchased from the commercial sources.

### Instrumentation

<sup>1</sup>H NMR spectra were recorded on a Bruker Avance 300 and 400 MHz spectrometer at room temperature in chloroform-*d* (CDCl<sub>3</sub>) purchased from Euriso-top. The conversion of prepared PNIPAM was analyzed by gas chromatography performed on an Agilent 7890A GC system from Agilent Technologies. Size-exclusion chromatography (SEC) was performed on an Agilent 1260-series HPLC system equipped with a 1260 online degasser, a 1260 ISO-pump, a 1260 automatic liquid sampler (ALS), a thermostatted column compartment (TCC) at 50 °C equipped with two PLgel 5 μm mixed-D columns and a mixed-D guard column in series, a 1260 diode array detector (DAD) and a 1260 refractive index detector (RID). The used eluent was DMA containing 50 mM LiCl at a flow rate of 0.500 mL min<sup>-1</sup>. The spectra were analyzed using the Agilent Chemstation software with the GPC add-on. The molar mass and dispersity values were calculated against PMMA standards from PSS. The morphologies of MnO<sub>2</sub> and PNIPAM@MnO<sub>2</sub> nanoparticles were determined by using a scanning electron microscope (FE-SEM, JEOL JSM-7100F) and a high-resolution transmission electron microscope (JEOL TEM 2100 Plus, Japan). Elemental analysis of samples was performed by X-ray photoelectron spectroscopy carried out on a PHI Versa Probe III scanning XPS microprobe (Physical Electronics, USA). The thermal behaviors of samples were measured with a Mettler Toledo TGA-DSC2/LF/1100 thermal gravimetric analyzer. The particle size distributions of products were characterized by a dynamic light scattering (DLS) instrument on a Malvern Zetasizer Nano Series operating a 4 mW He-Ne laser at 633 nm. The analysis was conducted over

a range of temperatures, from 10 to 50 °C, with a heating rate of 1.0 °C per minute, at an angle of 173°. Additionally, measurements were taken at a 90° scattering angle using a Zetasizer Malvern/Nano ZS-90 over different temperature range from 20 to 50 °C. UV-vis spectra were measured with a Cary 300 Bio UV-visible spectrophotometer. Temperature-responsive static fluorescence measurements were carried out on a Varian Cary Eclipse fluorescence spectrophotometer. A fluorescence spectrometer Edinburgh FLS 1000 was used to monitor fluorescence at various times in order to analyze the temperature-driven process.

## Methods

### Synthesis of nitrodopamine hydrogensulfate

Nitrodopamine hydrogensulfate was synthesized based on an established procedure.<sup>51</sup> A solution of dopamine hydrochloride (5.0 g, 26.4 mmol) and sodium nitrite (6.37 g, 92.3 mmol) in 150 mL distilled water was cooled to 0 °C using an ice bath. Aqueous sulphuric acid (50 mL, 20 v/v%) was slowly added to the reaction mixture. After the addition, the ice bath was removed and the solution was stirred overnight at room temperature. The resulting yellow dispersion was filtered using a sintered funnel and the collected solid was washed with ice-cold water several times and finally dried in a vacuum oven at 50 °C for 2 days to give nitrodopamine hydrogensulfate. <sup>1</sup>H NMR spectroscopy was used to confirm the nitrodopamine hydrogen sulfate structure (3.8 g, yield: 49%). A <sup>1</sup>H NMR spectrum of the nitrodopamine hydrogen sulfate is shown in Fig. S1.†

### Synthesis of pentafluorophenol (PFP) containing CTA

BTTCP-PFP was synthesized as described by Stenzel *et al.*<sup>52</sup> BTTCP (1.92 g, 8.1 mmol), PFP (1.60 g, 8.7 mmol) and DMAP (106 mg, 0.87 mmol) were added to a round-bottom flask and dissolved in anhydrous DCM (55 mL). The reaction mixture was cooled to 0 °C in an ice bath and a solution of DCC (1.80 g, 8.7 mmol) in DCM (15 mL) was added drop-wise with fast stirring. The reaction was allowed to stir in an ice bath for two hours and was continued at room temperature overnight. The resulting solution was filtered, and the solvent was evaporated under vacuum. The crude product was purified by column chromatography on silica gel using chloroform as the eluent. The solvent was removed under reduced pressure to obtain dark yellow oil (2.2 g, yield 67%). <sup>1</sup>H NMR spectroscopy was used to confirm the BTTCP-PFP structure as shown in Fig. S2.† <sup>1</sup>H-NMR (300 MHz, CDCl<sub>3</sub>) δ (ppm): 5.10 (q, *J* = 7.4, 1H, -CHCH<sub>3</sub>), 3.38 (t, *J* = 7.4 Hz, 2H, -SCH<sub>2</sub>-), 1.76 (d, *J* = 7.4 Hz, 3H, -CHCH<sub>3</sub>), 1.69 (tt, *J* = 7.4 Hz, 2H, -SCH<sub>2</sub>CH<sub>2</sub>-), 1.44 (app. sext, *J* = 7.4 Hz, 2H, -CH<sub>2</sub>CH<sub>3</sub>), 0.93 (t, *J* = 7.4 Hz, 3H, -CH<sub>2</sub>CH<sub>3</sub>).

### Synthesis of nitro DOPA-CTA

Nitro-dopamine (0.72 g, 3.58 mmol) was dispersed in DMF (5 mL) taken in a dry high-pressure test tube kept under an



argon atmosphere at room temperature. 1.1 mL of dry TEA was slowly added to the reaction mixture, which was left to stir for 10 minutes. Then BTTCP-PFP (1.02 g, 2.47 mmol) dissolved in DMF (5 mL) was added to the nitro-dopamine solution and left to stir at room temperature overnight. The reaction mixture was then dripped slowly into a phthalate buffer (150 mL, pH 3.0) to obtain a dark yellow dispersion and extracted with  $\text{CHCl}_3$ . The organic layer was dried over  $\text{Na}_2\text{SO}_4$  and filtered. Removal of the solvent under reduced pressure gave a crude product as a yellow liquid. (NB: traces of DMF were removed using heptane to make an azeotrope and concentrated at 50 °C under reduced pressure). The crude product was purified by column chromatography on silica gel using chloroform and ethyl acetate (3 : 1) as the eluent. After recrystallization from a toluene : hexane (50 : 50) mixture, the product was dried under vacuum to yield a solid yellow powder (0.67 g, 65% yield) (LC-MS  $[\text{M} - \text{H}]^- = 417.0$ ). A  $^1\text{H}$  NMR spectrum of the nitro DOPA-CTA is shown in Fig. S3.†

### Synthesis of PNIPAM-nitro DOPA

The RAFT polymerization of NIPAM was performed in a 25 mL Schlenk tube under an argon atmosphere. NIPAM (1.0 g, 8.84 mmol), butyl(1-((4,5-dihydroxy-2-nitrophenethyl)amino)-1-oxopropan-2-yl)carbonotrithioate (BDNAOCT) (37.0 mg, 0.09 mmol), 2,2'-azobisisobutyronitrile (AIBN) (7.3 mg, 0.044 mmol), and DMF (4.4 mL) were charged in the 25 mL Schlenk tube at a molar ratio of 100 : 1 : 0.5. The solution was deoxygenated by bubbling argon for 30 min. Then the reaction mixture was placed in a preheated oil bath at 60 °C to initiate the polymerization. After 145 min of polymerization, the Schlenk tube was removed from the oil bath and opened to the air and placed in ice to stop the polymerization. The resulting polymer was precipitated by dropping the polymer solution into 300 mL of cold diethyl ether. After decantation of some of the solvent, the polymer suspended in diethyl ether was centrifuged to isolate it.

Later the polymer was dispersed again in fresh diethyl ether and centrifuged again to isolate the polymer. The resulting powdery light-yellow polymer was dried for 2 days under vacuum at 50 °C. The monomer conversion was determined by GC whereas SEC was used to determine the molecular weight and dispersity ( $D$ ) (Fig. S4†) (conversion = 43%,  $M_{n\text{GC}} = 5.3$  kDa,  $DP = 43$ ;  $M_{n\text{SEC(DMA)}} = 10.9$  kDa and  $D = 1.09$ ).

### Synthesis of $\text{MnO}_2$ NPs

In a typical synthesis, a 20 mM solution of  $\text{KMnO}_4$  was prepared by dissolving 0.158 g (1 mmol) of  $\text{KMnO}_4$  in 25 mL of milliQ water, taken in a 250 mL conical flask. A second solution was prepared with 1.1 mL isoamyl alcohol dissolved in 25 mL of milliQ water. The isoamyl alcohol solution was added to the permanganate solution and the resulting reaction mixture was stirred at 700 rpm for 15 h at 25 °C. Then the resulting brown dispersed  $\text{MnO}_2$  nanoparticles were separated from the reaction mixture by centrifuging the mixture at 8000 rpm for 10 min and the residue was thoroughly washed with milliQ water 2 times, and finally suspended in 8.5 mL of

milliQ water. Later suspended  $\text{MnO}_2$  was dried and used for the next step. The obtained core-shell  $\text{MnO}_2$  NPs were characterized using UV-Vis, DLS, SEM, TEM, XPS, and TGA.

### Ligand-exchange with PNIPAM-nitro-DOPA

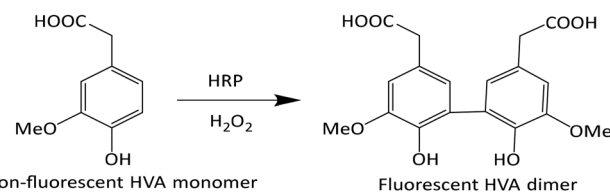
The  $\text{MnO}_2$  NPs (14.02 mg) were dispersed in 6 mL of dry DMF and PNIPAM-nitro-DOPA ( $M_n = 5.3$  kg mol $^{-1}$ ) (173.0 mg) was added in a 25 mL Schlenk tube. This solution was purged with argon, put in an ultrasonic bath for 30 min, shaken at room temperature for 44 h, ultrasonicated again for 40 min and precipitated in cold diethyl ether (180 mL). After centrifugation at 5000 rpm for 5 min, PNIPAM-modified  $\text{MnO}_2$  NPs were washed with diethyl ether and centrifuged again. The excess of diethyl ether was air dried and dispersed in milliQ water (180 mL). Later PNIPAM modified  $\text{MnO}_2$  nanoparticles were separated from the mixture by centrifugation at 8000 rpm for 10 min and the residue was thoroughly washed with milliQ water 3 times, and finally suspended in 8.5 mL of milliQ water. The obtained core-shell PNIPAM@ $\text{MnO}_2$  NPs were characterized using UV-Vis, DLS, SEM, TEM, XPS and TGA.

### HRP induced degradation of $\text{H}_2\text{O}_2$

Homovanillic acid/3-methoxy-4-hydroxyphenylacetic acid (HVA) is non-fluorescent; however, in combination with horse radish peroxidase (HRP) and  $\text{H}_2\text{O}_2$  a dimer is formed which is fluorescent (Scheme 1). Thus, an addition of HRP and HVA to a sample containing  $\text{H}_2\text{O}_2$  can be used to detect the presence of  $\text{H}_2\text{O}_2$ . A stock solution of HRP in PBS was made (3.41 mg enzyme dissolved in 1 mL buffer = 611 U mL $^{-1}$ ), which was combined with a 10 mM stock solution of HVA and  $\text{H}_2\text{O}_2$  in PBS.

### Effect of temperature on the degradation of $\text{H}_2\text{O}_2$ at 10 and 50 °C

For the investigation of temperature effect on the degradation of  $\text{H}_2\text{O}_2$  at 10 and 50 °C, 950  $\mu\text{L}$  of PBS and 50  $\mu\text{L}$  of  $\text{H}_2\text{O}_2$  were added to an Eppendorf cuvette and placed in the thermoshaker at 10 °C and 50 °C, respectively. Once the Eppendorf reached those temperatures, 10  $\mu\text{L}$  of the NP solution was added and left to react for 10 min then the Eppendorf was centrifuged at 4 °C (7500 rpm, 10 min) in order to precipitate the NP. 750  $\mu\text{L}$  of the supernatant was taken and added to a cuvette together with 50  $\mu\text{L}$  of HRP, 100  $\mu\text{L}$  of HVA, and 1600  $\mu\text{L}$  of PBS and investigated using a fluorometric method. The same experiment was done in parallel but without the addition of the NP solution, as the reference.



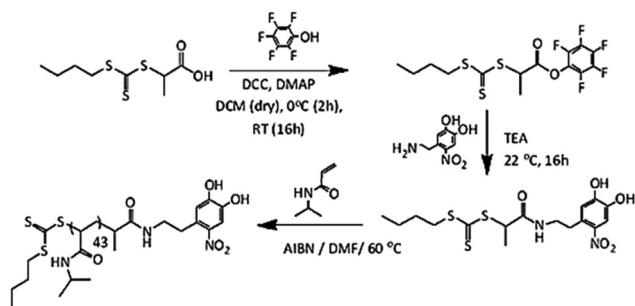
**Scheme 1** Dimerization of HVA by the action of HRP and  $\text{H}_2\text{O}_2$ .



## Results and discussion

Poly(*N*-isopropyl acrylamide) (PNIPAM) is a frequently studied thermoresponsive polymer due to its cloud point temperature of about 32 °C, which is quite close to human body temperature. The synthesis of well-defined nitro-dopamine end-functionalized PNIPAM was performed by reversible addition fragmentation chain-transfer (RAFT) polymerization. Therefore, nitrodopamine hydrogensulfate was reacted with pentafluorophenol (PFP) containing CTA to obtain butyl(1-((4,5-dihydroxy-2-nitrophenethyl)amino)-1-oxopropan-2-yl)carbonotrithioate (BDNAOCT) chain transfer agent (CTA). <sup>1</sup>H-NMR spectroscopy was used to confirm its structure (Fig. S3†). The polymer was subsequently synthesized in DMF at 60 °C in the presence of AIBN utilizing BDNAOCT as the RAFT chain transfer agent (CTA) (Scheme 2). At around 43% conversion, the polymerization was stopped and the formed polymer was isolated by precipitation in cold diethyl ether. Theoretical molecular weight and the degree of polymerization (DP) were calculated and found to be 5.3 kDa and 43, respectively. SEC results of the synthesized polymer revealed that the polymer is well defined with  $M_n$  and dispersity ( $D$ ) at 10.9 kDa and 1.09, respectively (Fig. S4†). MnO<sub>2</sub> NPs were prepared by mixing KMnO<sub>4</sub> with isoamyl alcohol using the procedure reported in the literature.<sup>53</sup> In this method KMnO<sub>4</sub> acts as an oxidizing agent that eventually oxidizes the alcohol to the corresponding acid, which caps the spherical MnO<sub>2</sub> particles. The purple colour of the KMnO<sub>4</sub> solution resulting from the charge transfer (CT) transition turns into a yellowish-brown colour when it transforms into MnO<sub>2</sub> NPs (Fig. S5†). The optical properties of the MnO<sub>2</sub> NPs in water were investigated and compared with the starting KMnO<sub>4</sub>. It was observed that the characteristic absorption bands of KMnO<sub>4</sub> at  $\lambda = 508, 526, 546,$  and  $565$  nm resulting from the CT transition vanish and a new broad peak was observed in the range of 300–450 nm, indicating the formation of MnO<sub>2</sub> NPs as evident from Fig. 2a. From the DLS measurement of prepared MnO<sub>2</sub> NPs, the average particle size was confirmed to be around 278.5 nm measured at 25 °C (Fig. 2b).

Next, PNIPAM@MnO<sub>2</sub> NPs were prepared by ligand-exchange, which was achieved by shaking the solution of MnO<sub>2</sub> NPs and PNIPAM in DMF for 2 days. The resulting



**Scheme 2** Schematic representation of the synthesis of dopamine-functionalized PNIPAM.

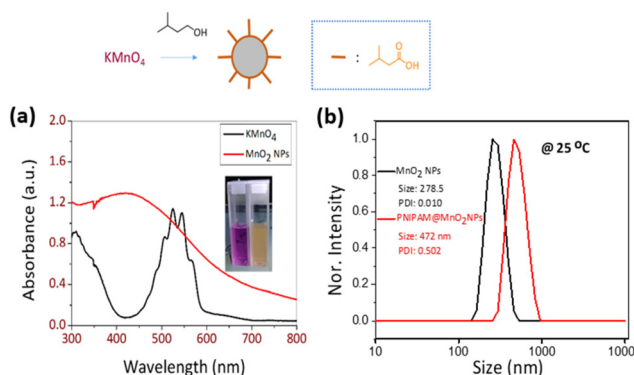


**Fig. 2** (a) UV-vis spectra of KMnO<sub>4</sub> and MnO<sub>2</sub> NPs and (b) size distribution obtained from DLS of MnO<sub>2</sub> NPs and PNIPAM@MnO<sub>2</sub> NPs. It should be noted that the x-axis is on the logarithmic scale.

PNIPAM@MnO<sub>2</sub> NPs was isolated by precipitation in cold DEE followed by centrifugation leading to a solid sample that could be redispersed in water for future investigations (Fig. S6†). The mechanism of surface modification of MnO<sub>2</sub> by nitrodopamine is elaborately discussed by Sivakumar *et al.*,<sup>26</sup> as mentioned earlier. Both theoretical and experimental proofs are given to prove the attachment of catechol hydroxyl groups present in nitrodopamine to the MnO<sub>2</sub> surface. The strong electron withdrawing nitro group in nitrodopamine makes the catechol hydroxyl more acidic and thus favours the effective binding on the surface of NPs. DLS analysis of the PNIPAM@MnO<sub>2</sub> NPs revealed an increase of the size to 472 nm, confirming the presence of the polymer coating, while the PDI was at 0.502 (Fig. 2b). SEM images of the MnO<sub>2</sub> NPs and the PNIPAM@MnO<sub>2</sub> NPs are shown in Fig. 3. Fig. 3a shows well-dispersed MnO<sub>2</sub> NPs with a particle size around the 200–300 nm range as given in Fig. S7a.† The size of the PNIPAM@MnO<sub>2</sub> NPs clearly shows an increase in the particle size after polymer modification as shown in Fig. 3b, albeit the

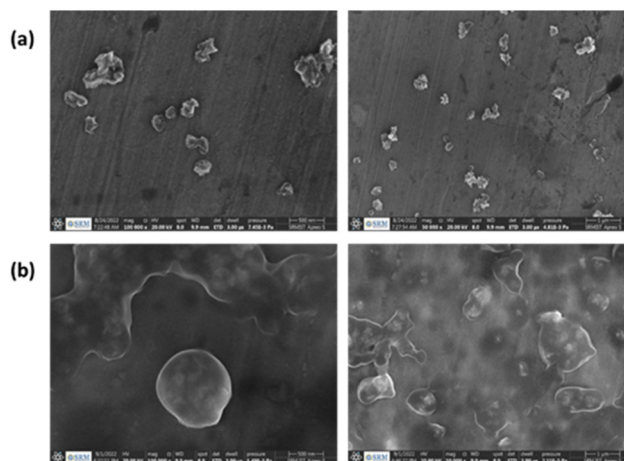


**Fig. 3** (a) SEM image of MnO<sub>2</sub> NPs (scale bar is 500 nm; right: scale bar is 1 μm), (b) SEM image of PNIPAM@MnO<sub>2</sub> NPs (scale bar is 500 nm; right: scale bar is 1 μm).



image becomes more blurry in the presence of the polymer coating and the resolution of the SEM analysis is insufficient to visualize the polymer coating. Furthermore, it is evident that the  $\text{MnO}_2$  NPs are coated by the polymer individually or in the agglomerated stage, which is mostly likely due to the dehydration of the polymer during the sample preparation process as DLS confirmed the presence of defined individual particles. In Fig. 3b (right) the particle size was determined to be around 400–600 nm given in Fig. S7b.† Therefore, it is clear that PNIPAM is coated on to the NP surfaces. By using energy-dispersive X-ray (EDX) analysis, we have determined the elemental composition (Fig. 4a). The presence of Mn and oxygen peaks corroborates well with the elemental composition, as shown in Table S1.† Furthermore, the EDX analysis of the PNIPAM@ $\text{MnO}_2$  NPs shows an enhancement in carbon percentage and the presence of other elements, such as nitrogen and sulphur, in agreement with the polymer coating (Fig. 4b and Table S2.†). As the surface of the NPs is modified with the polymer, the Mn composition on the surface is declined, confirming successful polymer coating of the  $\text{MnO}_2$  NPs.

TEM images of the synthesized  $\text{MnO}_2$  NPs showed the flaky structure with microfibrillar morphology. It is evident from a comparison of the images of unmodified and modified nanoparticles (Fig. 5a and b, respectively) that the modified NPs have a visible polymer coating layer.

X-ray photoelectron spectroscopy was used to perform a basic investigation to identify the corresponding valence states of the materials. Overall the XPS spectra of the  $\text{MnO}_2$  NPs showed peaks corresponding to all the elements with characteristic valence states as expected in the sample (Fig. 6a). Giving further attention to each element, Mn 2p and O 1s XPS spectra are shown in Fig. 6b and c, respectively. In the deconvoluted Mn 2p peak, the two peaks observed at 654.10 and 642.34 eV with an energy separation of 11.76 eV correspond to the Mn 2p<sub>3/2</sub> and Mn 2p<sub>1/2</sub> orbitals (Fig. 6b). Similarly, the O 1s peak of  $\text{MnO}_2$  was curve-fitted as shown in Fig. 6c, and includes three characteristic oxygen bonds, which are associated to the Mn–O–Mn bond, Mn–O–H bond and H–O–H bond with binding energies (BEs) of 529.73 eV, 530.97 eV and 533.08 eV, respectively. Previously reported values of the XPS spectra for the oxidation state of Mn and O in the  $\text{MnO}_2$  NPs agree well with these findings.<sup>54,55</sup>

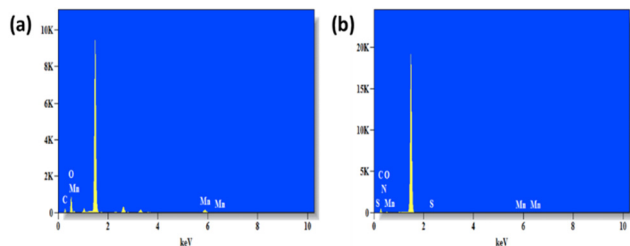


Fig. 4 (a) EDX graph of  $\text{MnO}_2$  NPs and (b) EDX graph of PNIPAM@ $\text{MnO}_2$  nanoparticles.

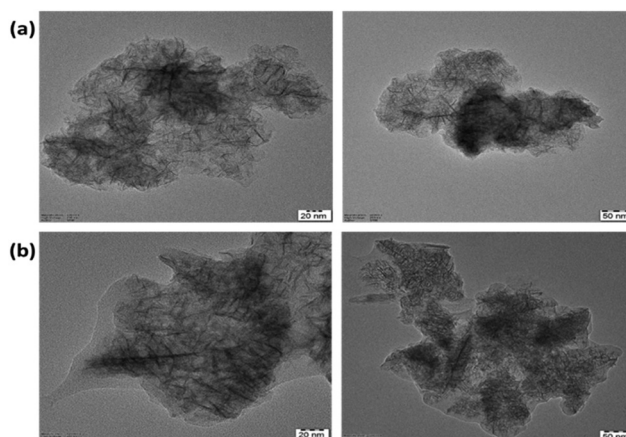


Fig. 5 (a) TEM micrographs of dispersed  $\text{MnO}_2$  nanoparticles (scale bar is 20 nm; right: scale bar is 50 nm; the zoomed image shows a  $\text{MnO}_2$  nanoparticle with a microfibrillar structure), (b) TEM micrographs of dispersed PNIPAM@ $\text{MnO}_2$  nanoparticles (scale bar is 20 nm; right: scale bar is 50 nm; the zoomed image shows a  $\text{MnO}_2$  nanoparticle with a microfibrillar structure).

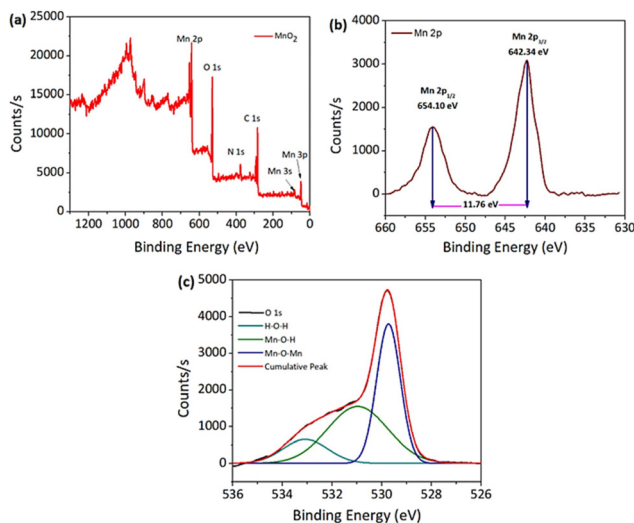


Fig. 6 XPS spectra. (a) Overall  $\text{MnO}_2$  NPs and (b) Mn 2p and (c) O 1s orbitals.

For the PNIPAM@ $\text{MnO}_2$  NPs, the overall XPS spectrum showed (Fig. S8a†) an increase in the elemental composition of carbon and nitrogen, whereas a drastic decrease in the Mn composition confirms the successful coating of PNIPAM onto the nanoparticles. Fig. S8b and S8c† corresponding to the Mn 2p and O 1s orbitals provide similar deconvoluted peaks as that of the unmodified NPs, but with a lower count of elements due to the enhancement of carbon and nitrogen composition from the polymer.

Nonetheless, the presence of Mn and O is evident from the spectra. Carbon (C 1s) high resolution spectra from PNIPAM were resolved by curve-fitting into five component peaks (Fig. S8d†). The peak with a BE of 284.24 eV corresponds to



the C=C bonds associated with the aromatic end-group of the polymer. A peak with a BE at 285.01 eV corresponds to the C-H/C-C bonds with the aliphatic hydrocarbon part of the polymer. Other peaks with a BE at 286.27, 287.15 and 287.59 eV are attributed to the C-O/C-S, N-C=O and C=O bonds, respectively. Similar spectra and binding environments (C-H/C-C, C=C, C-O/C-S, N-C=O and C=O) were observed for the C 1s orbital in other literature studies.<sup>56–58</sup> Fig. S8e† shows the deconvoluted peaks of the N 1s orbital and the peaks observed at 399 eV and 400 eV are attributed to the C-N and N-O bonds respectively.<sup>59,60</sup> Three peaks appeared in the expanded spectra of the S 2p orbital (Fig. S8f†). The first peak can be ascribed to sulphur atoms bound with carbon by C=S double bonds at 164 eV; also a small amount of oxidized sulphur was observed at 168.5 eV.<sup>61</sup>

Thermal gravimetric analysis (TGA) also showed the successful coating of PNIPAM onto the MnO<sub>2</sub> NP surface (Fig. S9†). The TGA analysis of the PNIPAM@MnO<sub>2</sub> NPs showed a two-step weight loss at 190 °C and 400 °C, which is due to the PNIPAM coating on the nanoparticles. The observation of a second decomposition at ~400 °C of the polymer is in good agreement with that of pure PNIPAM.<sup>62</sup> The TGA curve of pure MnO<sub>2</sub> possesses only one weight loss step due to the loss of moisture from an MnO<sub>2</sub> lattice (adsorbed water molecules).<sup>63</sup>

Dynamic light scattering (DLS) data indicated that the synthesized MnO<sub>2</sub> NPs were stable and well dispersed in an aqueous medium with an average particle size of 278.5 nm and a polydispersity index (PDI) of 0.010 (Fig. S10†). The particle size was remeasured after 15 days and found to be stable at 25 °C. Temperature-dependent aggregation of the MnO<sub>2</sub> NPs was also investigated by DLS in an aqueous medium (Fig. S10†). The particle size of the MnO<sub>2</sub> NPs remained almost unchanged at 25 °C (278 nm) and 50 °C (287 nm) indicating the absence of temperature-dependent aggregation of unmodified NPs. In contrast with the MnO<sub>2</sub> NPs, the PNIPAM@MnO<sub>2</sub> NPs showed temperature-responsive behavior when measured at 25 °C, 35 °C, and 50 °C, respectively (Fig. 7a). Upon increasing the temperature from 25 °C to 35 °C, a decrease in the particle size of 127 nm was observed from 472 nm to 345 nm. By further heating above the LCST of

PNIPAM at 50 °C, an increment of 157 nm in the particle size was detected. In order to obtain additional information on the temperature-responsive behaviour of the PNIPAM@MnO<sub>2</sub> NPs, DLS measurement was analysed in 5 °C intervals from 20 to 50 °C. The change in the diameter of the NPs with temperature can be seen from the graphs plotted in Fig. 7a. At the  $T_{cp}$  of PNIPAM at around 35 °C there is a drop in the diameter when compared to the lower and higher temperatures. At the lower temperature the polymer chains are efficiently hydrated, leading to a larger hydrodynamic diameter. When the temperature approaches the  $T_{cp}$ , the polymer chains are dehydrated and collapse onto the individual NPs, resulting in a decrease in the observed particle size. Upon further heating, the particle size gradually increases as, at temperatures above the  $T_{cp}$  of PNIPAM, the polymer chains are further dehydrated and collapse, inducing hydrophobic interactions that lead to the aggregation of polymer modified NPs. The size reaches a maximum of 579 nm at around 42 °C, followed by a slight decline due to the precipitation of aggregated particles (Fig. 7b).

The observed changes in the particle size with temperature suggest that PNIPAM@MnO<sub>2</sub> NPs can be used as smart material for the catalytic decomposition of H<sub>2</sub>O<sub>2</sub>, based on the dehydration of PNIPAM at increased temperatures.

To investigate the effect of nanoparticle concentration on the temperature-induced aggregation and temperature-induced reversibility of the smart PNIPAM@MnO<sub>2</sub> NPs, we lowered the concentration of the nanoparticles to half, leading to an increase in the particle size to 580 nm at 20 °C, indicating more efficient polymer hydration (Fig. S11a†). At this lower concentration, we did not observe NP aggregation above the  $T_{cp}$  of PNIPAM. Instead, the particle size decreased to around 240 nm upon heating to 50 °C, indicating the collapse of the dehydrated polymer chains onto the NPs without any further aggregation. The temperature-induced dehydration of the PNIPAM coating at this lower concentration was also found to be reversible without noticeable deviations during five cycles (Fig. S11b†).

To investigate the temperature effect on the catalytic activity of the developed smart NPs, fluorescence experiments were conducted at three different temperatures, 10, 37, and 50 °C, respectively. As illustrated in Scheme 1, the non-fluorescent HVA monomer is transformed into the fluorescent HVA dimer (2,2'-dihydroxy-3,3'-dimethoxydiphenyl-5,5'-diacetic acid) in the presence of HRP and H<sub>2</sub>O<sub>2</sub>, resulting in enhanced fluorescence. The strong reactivity of H<sub>2</sub>O<sub>2</sub> with transition metal-containing heme peroxides, such as HRP, has been reported to result in high-rate constants, in the range of 10<sup>7</sup>–10<sup>8</sup> M<sup>-1</sup> s<sup>-1</sup>.<sup>64</sup> The resulting metal-containing heme peroxide complex catalyzes the dimerization of HVA into the fluorescent dimer. We have successfully utilized this method to investigate the activity of H<sub>2</sub>O<sub>2</sub> in the presence of the smart PNIPAM@MnO<sub>2</sub> NPs at different temperatures. Therefore, the change in the fluorescent intensity at 10 and 50 °C in the presence and absence of PNIPAM@MnO<sub>2</sub> NPs was analysed as shown in Fig. S12.†

The fluorescence studies were carried out at two different temperatures, 10 °C and 50 °C, respectively, in order to investi-

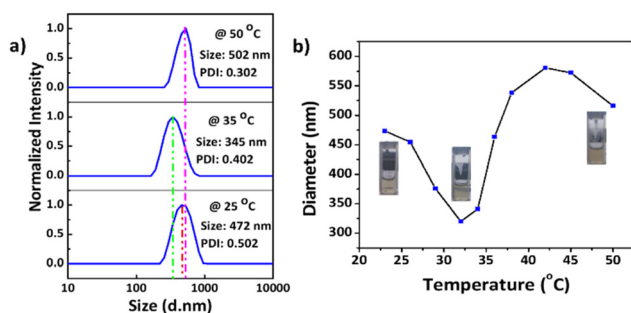


Fig. 7 (a) Particle size and PDI of the PNIPAM@MnO<sub>2</sub> NPs at three different temperatures: 25 °C, 35 °C and 50 °C, respectively; (b) change in particle sizes with temperature varying from 23 to 50 °C at a concentration of 0.2 mg mL<sup>-1</sup> in all cases.



gate the influence of temperature on the catalytic activity of the PNIPAM@MnO<sub>2</sub> NPs for the decomposition of H<sub>2</sub>O<sub>2</sub> (Fig. 8). These two temperatures are taken into account for our analysis since these are below and above the  $T_{cp}$  of PNIPAM ( $T_{cp} \sim 32$  °C). Note that we used a reverse assay to monitor the remaining H<sub>2</sub>O<sub>2</sub> through HRP catalysed dimerization of HVA, leading to significant background fluorescence at  $t = 0$  due to the presence of all reactive components before the addition of the PNIPAM@MnO<sub>2</sub> NPs.

After 15 min in the presence of PNIPAM@MnO<sub>2</sub> NPs, the fluorescence intensity only increased from 385 a.u. to 442 a.u. ( $\lambda_{em,max}@t_{15}/\lambda_{em,max}@t_0 = 1.15$ ) at 10 °C, while in the absence of PNIPAM@MnO<sub>2</sub> NPs the fluorescence intensity increased from 330 a.u. to 588 a.u. ( $\lambda_{em,max}@t_{15}/\lambda_{em,max}@t_0 = 1.78$ ) during the same time interval. This result clearly demonstrates less dimer formation indicative of a lower H<sub>2</sub>O<sub>2</sub> concentration, implying that H<sub>2</sub>O<sub>2</sub> is catalytically decomposed in the presence of the PNIPAM@MnO<sub>2</sub> NPs. In contrast, at 50 °C, the fluorescence intensity increased from 341 to 529 a.u. ( $\lambda_{em,max}@t_{15}/\lambda_{em,max}@t_0 = 1.55$ ) in the presence of the PNIPAM@MnO<sub>2</sub> NPs, while in the absence of PNIPAM@MnO<sub>2</sub> NPs it increased from 334 a.u. to 632 a.u. ( $\lambda_{em,max}@t_{15}/\lambda_{em,max}@t_0 = 1.89$ ) for the same time interval. As a result, it was evident that the increase in relative fluorescence intensity in the presence of smart NPs is much higher at 50 °C than at 10 °C. As this temperature is above the LCST of PNIPAM ( $\sim 32$  °C) it induces dehydration and collapse of the PNIPAM chains onto the NPs, preventing the catalyst from coming into contact with the H<sub>2</sub>O<sub>2</sub>, resulting in higher retention of the H<sub>2</sub>O<sub>2</sub> and, thus, in greater fluorescence increase due to HVA dimer formation. Control experiments at 37 °C revealed that there is no fluorescence increase without H<sub>2</sub>O<sub>2</sub>, but there is a moderate increase in fluorescence in the presence of H<sub>2</sub>O<sub>2</sub>, and a strong increase in fluorescence in the presence of both H<sub>2</sub>O<sub>2</sub> and HRP (Fig. S13<sup>†</sup>).

Furthermore, we have investigated the role of H<sub>2</sub>O<sub>2</sub> towards the dimerization of HVA in the absence of the PNIPAM@MnO<sub>2</sub>

NPs (Fig. S14<sup>†</sup>), indicating a strong correlation of fluorescence intensity increase with the H<sub>2</sub>O<sub>2</sub> concentration, further supporting the observed temperature-switchable catalytic activity of the PNIPAM@MnO<sub>2</sub> NPs.

## Conclusions

In this work we have successfully synthesized and characterized temperature responsive PNIPAM coated MnO<sub>2</sub> NPs for the catalytic decomposition of H<sub>2</sub>O<sub>2</sub>. Successful coating of the NP surface with nitrodopamine functionalized PNIPAM was confirmed by the analysis of elemental compositions, SEM and XPS. The results were further confirmed by TEM images, as a clear uniform coating of polymers on NPs is visible from the images. The TGA results validated the PNIPAM coating on the surface of MnO<sub>2</sub> NPs. The synthesized PNIPAM@MnO<sub>2</sub> NPs were proved to be temperature-responsive by DLS and fluorescence spectroscopy. Thermoresponsive swelling and deswelling of PNIPAM@MnO<sub>2</sub> NPs were confirmed as the particle size of the nanoparticles altered with the change in temperature. The catalytic decomposition of H<sub>2</sub>O<sub>2</sub> by MnO<sub>2</sub> is a renowned exothermic reaction. This reaction is done with the synthesized PNIPAM@MnO<sub>2</sub> NPs and a fluorescence assay for HVA dimerization proved the significant catalytic decomposition of H<sub>2</sub>O<sub>2</sub> at a lower temperature (below the  $T_{cp}$  of PNIPAM) by the PNIPAM@MnO<sub>2</sub> NPs. At a higher temperature (above the  $T_{cp}$  of PNIPAM), H<sub>2</sub>O<sub>2</sub> decomposition was found to be less significant. These results confirm that the smart nanoparticles can be used for the temperature-dependent catalytic decomposition of H<sub>2</sub>O<sub>2</sub>. In the future, we aim to further develop this system towards self-regulated smart catalytic systems.

## Data availability

The data supporting this article have been included in the main manuscript and as part of the ESI.<sup>†</sup>

## Author contributions

The manuscript was written through the contributions of all authors. All authors have given approval to the final version of the manuscript.

## Conflicts of interest

There are no conflicts to declare.

## Acknowledgements

A. B. and G. S. thanks SRMIST for providing the fellowship to support the Ph.D. program. S. M. acknowledges SRMIST for providing the SRMIST seed grant, the Science and Engineering

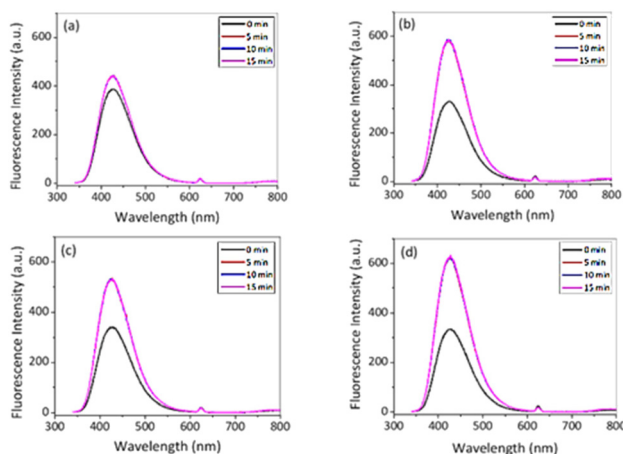


**Fig. 8** Fluorescence intensity in the presence of HVA, HRP and 50  $\mu$ L of H<sub>2</sub>O<sub>2</sub> (a) with NPs; (b) without NPs at 10 °C and (c) with NPs; and (d) without NPs at 50 °C in PBS ( $\lambda_{ex} = 312$  nm).





Research Board (SERB), India, for a core research grant (CRG/2021/004203) and FWO. R. H. thanks FWO and Ghent University for financial support. We thank Dr. Vincent Ornelis from UGent, Belgium, for the measurement of PL of PNIPAM@MnO<sub>2</sub>NP samples and Ms Sushma Kundu from TIFR Mumbai, India, for TGA measurements.

## References

- N. Di Marzo, E. Chisci and R. Giovannoni, *Cells*, 2018, **7**, 156.
- L. Zhang, C. Jia, F. Bai, W. Wang, S. An, K. Zhao, Z. Li, J. Li and H. Sun, *Fuel*, 2024, **355**, 129455.
- R. J. Lewis and G. J. Hutchings, *Acc. Chem. Res.*, 2024, **57**, 106–119.
- Z. Wang, L. Peng, P. Zhu, W. Wang, C. Yang, H.-Y. Hu and Q. Wu, *ACS Nano*, 2024, **18**, 2885–2897.
- B. Kichatov, A. Korshunov, V. Sudakov, A. Golubkov, D. Smovzh, S. Sakhapov and M. Skirda, *Phys. Chem. Chem. Phys.*, 2024, **26**, 1612–1615.
- J. J. Dolhun, *J. Chem. Educ.*, 2014, **91**, 760–762.
- T. Zeng, X. Meng, S. Sun, M. Ling, C. Zhang, W. Yuan, D. Cao, M. Niu, L. Y. Zhang and C. M. Li, *Small Methods*, 2023, **7**, 2300791.
- X. Zhang, G. Zhu, B. Xiao, J. Geng, Y. Yang, D. Wang, J. Li, J. Wang and Y. Zhu, *Sep. Purif. Technol.*, 2024, **330**, 125338.
- B. Martin, J. Sedelmeier, A. Bouisseau, P. Fernandez-Rodriguez, J. Haber, F. Kleinbeck, S. Kamptmann, F. Susanne, P. Hoehn, M. Lanz, L. Pellegatti, F. Venturoni, J. Robertson, M. C. Willis and B. Schenkel, *Green Chem.*, 2017, **19**, 1439–1448.
- Z.-L. Wu, C.-K. Li, J.-G. Yu and X.-Q. Chen, *Sens. Actuators, B*, 2017, **239**, 544–552.
- K. Sobańska, P. Pietrzyk and Z. Sojka, *ACS Catal.*, 2017, **7**, 2935–2947.
- M. J. Männel, L. P. Kreuzer, C. Goldhahn, J. Schubert, M. J. Hartl and M. Chanana, *ACS Catal.*, 2017, **7**, 1664–1672.
- L. P. Kreuzer, M. J. Männel, J. Schubert, R. P. M. Höller and M. Chanana, *ACS Omega*, 2017, **2**, 7305–7312.
- Y. Wu, P. Balasubramanian, Z. Wang, J. A. S. Coelho, M. Prslja, R. Siebert, M. B. Plenio, F. Jelezko and T. Weil, *J. Am. Chem. Soc.*, 2022, **144**, 12642–12651.
- C. Busquets-Cortés, X. Capó, E. Argelich, M. Ferrer, D. Mateos, C. Bouzas, M. Abbate, J. Tur, A. Sureda and A. Pons, *Nutrients*, 2018, **10**, 1920.
- M. Zhu, L. Zhu, Y. You, M. Sun, F. Jin, Y. Song, J. Zhang, X. Xu, J. Ji and Y. Du, *ACS Nano*, 2023, **17**, 17285–17298.
- H. J. Forman and H. Zhang, *Nat. Rev. Drug Discovery*, 2021, **20**, 689–709.
- S. Mourdikoudis, R. M. Pallares and N. T. K. Thanh, *Nanoscale*, 2018, **10**, 12871–12934.
- M. Hermanek, R. Zboril, I. Medrik, J. Pechousek and C. Gregor, *J. Am. Chem. Soc.*, 2007, **129**, 10929–10936.
- M. Xu, Y. Wang, J. Yang, J. Wang, D. Liu, L. Zhou and H. Liu, *Sep. Purif. Technol.*, 2024, **330**, 125263.
- S. Sisakhtnezhad, M. Rahimi and S. Mohammadi, *Biomed. Pharmacother.*, 2023, **163**, 114833.
- Y. Yang, K. Hu, Z. Zhu, Y. Yao, P. Zhang, P. Zhou, P. Huo, X. Duan, H. Sun and S. Wang, *Small Methods*, 2023, **7**, 2300588.
- J. P. C. Moura, V. S. Antonin, A. B. Trench and M. C. Santos, *Electrochim. Acta*, 2023, **463**, 142852.
- M. Song, T. Liu, C. Shi, X. Zhang and X. Chen, *ACS Nano*, 2016, **10**, 633–647.
- A. Matsugi, *Combust. Flame*, 2021, **225**, 444–452.
- G. Sivakumar, A. Gupta, A. Babu, P. K. Sasmal and S. Maji, *J. Mater. Chem. B*, 2024, **12**, 4724–4735.
- H. G. Schild, *Prog. Polym. Sci.*, 1992, **17**, 163–249.
- L. Johnson, D. M. Gray, E. Niezabitowska and T. O. McDonald, *Nanoscale*, 2021, **13**, 7879–7896.
- A. Das, A. Babu, S. Chakraborty, J. F. R. Van Guyse, R. Hoogenboom and S. Maji, *Adv. Funct. Mater.*, 2024, 2402432.
- R. Wang, Q. Wei, W. Sheng, B. Yu, F. Zhou and B. Li, *Angew. Chem., Int. Ed.*, 2023, **62**, e202219312.
- K. Matyjaszewski, *Macromolecules*, 2012, **45**, 4015–4039.
- K. Matyjaszewski and J. Xia, *Chem. Rev.*, 2001, **101**, 2921–2990.
- J.-S. Wang and K. Matyjaszewski, *J. Am. Chem. Soc.*, 1995, **117**, 5614–5615.
- C. J. Hawker, A. W. Bosman and E. Harth, *Chem. Rev.*, 2001, **101**, 3661–3688.
- J. Nicolas, Y. Guillaneuf, C. Lefay, D. Bertin, D. Gigmès and B. Charleux, *Prog. Polym. Sci.*, 2013, **38**, 63–235.
- G. Vancoillie, S. Pelz, E. Holder and R. Hoogenboom, *Polym. Chem.*, 2012, **3**, 1726–1729.
- S. Perrier, *Macromolecules*, 2017, **50**, 7433–7447.
- G. Moad, *Polym. Chem.*, 2017, **8**, 177–219.
- X. Tian, J. Ding, B. Zhang, F. Qiu, X. Zhuang and Y. Chen, *Polymers*, 2018, **10**, 318.
- C. Sánchez-Rodríguez, R. Palao-Suay, L. Rodríguez, M. Aguilar, S. Martín-Saldaña, J. San Román and R. Sanz-Fernández, *Biomolecules*, 2018, **8**, 97.
- S. Maji, G. Vancoillie, L. Voorhaar, Q. Zhang and R. Hoogenboom, *Macromol. Rapid Commun.*, 2014, **35**, 214–220.
- S. Maji, Z. Zhang, L. Voorhaar, S. Pieters, B. Stubbe, S. Van Vlierberghe, P. Dubrue, B. G. De Geest and R. Hoogenboom, *RSC Adv.*, 2015, **5**, 42388–42398.
- M. Chen, M. Zhong and J. A. Johnson, *Chem. Rev.*, 2016, **116**, 10167–10211.
- D. A. Gkika, A. K. Tolkou, D. A. Lambropoulou, D. N. Bikiaris, P. Kokkinos, I. K. Kalavrouziotis and G. Z. Kyzas, *RSC Appl. Polym.*, 2024, **2**, 127–148.
- D. Roy, W. L. A. Brooks and B. S. Sumerlin, *Chem. Soc. Rev.*, 2013, **42**, 7214.
- C. Boutris, E. G. Chatzi and C. Kiparissides, *Polymer*, 1997, **38**, 2567–2570.
- S. Maji, B. Cesur, Z. Zhang, B. G. De Geest and R. Hoogenboom, *Polym. Chem.*, 2016, **7**, 1705–1710.



- 48 A. Babu, G. Sivakumar, M. Anandan, P. Adhya, T. Akash, T. Mondal, V. Nutalapati and S. Maji, *Eur. Polym. J.*, 2023, **200**, 112527.
- 49 M. A. Cooperstein and H. E. Canavan, *Langmuir*, 2010, **26**, 7695–7707.
- 50 C. J. Ferguson, R. J. Hughes, D. Nguyen, B. T. T. Pham, R. G. Gilbert, A. K. Serelis, C. H. Such and B. S. Hawkett, *Macromolecules*, 2005, **38**, 2191–2204.
- 51 S. Kurzhals, R. Zirbs and E. Reimhult, *ACS Appl. Mater. Interfaces*, 2015, **7**, 19342–19352.
- 52 W. Scarano, H. Lu and M. H. Stenzel, *Chem. Commun.*, 2014, **50**, 6390–6393.
- 53 A. K. Sinha, M. Basu, M. Pradhan, S. Sarkar, Y. Negishi and T. Pal, *J. Phys. Chem. C*, 2010, **114**, 21173–21183.
- 54 G. Xie, X. Liu, Q. Li, H. Lin, Y. Li, M. Nie and L. Qin, *J. Mater. Sci.*, 2017, **52**, 10915–10926.
- 55 J. M. de O. Cremonozzi, D. Y. Tiba and S. H. Domingues, *SN Appl. Sci.*, 2020, **2**, 1689.
- 56 A. Munir, T. ul Haq, A. Qurashi, H. ur Rehman, A. Ul-Hamid and I. Hussain, *ACS Appl. Energy Mater.*, 2019, **2**, 363–371.
- 57 P. Shivapooja, L. K. Ista, H. E. Canavan and G. P. Lopez, *Biointerphases*, 2012, **7**, 32.
- 58 X. Yang, Z. Sun, J. Gao, C. Yang and D. Tang, *Polym. Bull.*, 2020, **77**, 963–974.
- 59 A. Agrawal, K. Biswas, S. K. Srivastava and S. Ghosh, *J. Solid State Electrochem.*, 2018, **22**, 3443–3455.
- 60 X. Yan, T. Xu, G. Chen, S. Yang, H. Liu and Q. Xue, *J. Phys. D: Appl. Phys.*, 2004, **37**, 907–913.
- 61 N. Fechner, T.-P. Fellingner and M. Antonietti, *J. Mater. Chem. A*, 2013, **1**, 14097.
- 62 L. Wang, Y. Wu, Y. Men, J. Shen and Z. Liu, *RSC Adv.*, 2015, **5**, 70758–70765.
- 63 S. Mallakpour, A. Abdolmaleki and H. Tabebordbar, *Polym. Bull.*, 2017, **74**, 2957–2973.
- 64 X. Huang and J. T. Groves, *Chem. Rev.*, 2018, **118**, 2491–2553.

